Differential cross section for n-p elastic scattering in the angular range $51° < \theta^* < 180°$ at 647.5 MeV

M. L. Evans,* G. Glass, J. C. Hiebert, Mahavir Jain,†
R. A. Kenefick, and L. C. Northcliffe
Texas A&M University, College Station, Texas 77843

B. E. Bonner and J. E. Simmons
Los Alamos National Laboratory, Los Alamos, New Mexico 87545

C. W. Bjork† and P. J. Riley
University of Texas, Austin, Texas 78712

H. C. Bryant, C. G. Cassapakis,‡ B. Dieterle, C. P. Leavitt,
and D. M. Wolfe
University of New Mexico, Albuquerque, New Mexico 87131

D. W. Werren§
University of Geneva, Geneva, Switzerland
(Received 30 July 1982)

The n-p elastic differential cross section in the angular range $51° < \theta^* < 180°$ at 647.5 MeV has been measured with high statistical precision, good relative accuracy, and absolute normalization of 7% estimated accuracy (based on the observed yield of deuterons from $np \rightarrow d\pi^0$). A monoenergetic neutron beam bombarded a liquid hydrogen target, and the protons and deuterons ejected from the target were detected by a multiwire proportional chamber spectrometer which measured their momentum, angle, and mass. The results resolve discrepancies between previous measurements of this observable, and are in reasonable agreement with Saclay data at large angles, and with a phase shift fit. Evidence for accuracy of the shape of the angular distribution is provided by the good value obtained for the pion-nucleon coupling constant ($f^2 = 0.0759 \pm 0.0030$) when the pole-extrapolation method of Chew is used to extract f^2 from this shape.

[NUCLEAR REACTIONS ^{1}H(n,p)n, $T_n = 674.5$ MeV; measured $d\sigma/d\Omega^*$ vs θ^* for $51° < \theta^* < 180°$.]

I. INTRODUCTION

A determination of the interaction between neutron and proton continues to be one of the most fundamental but incompletely solved problems in medium energy nuclear physics. Much progress has been made in recent years, however, and the unambiguous determination of the n-p isoscalar ($I = 0$) interaction for energies up to 425 MeV found earlier by Arndt *et al.*[1] has been confirmed and extended up to 550 MeV in a current analysis by DuBois *et al.*[2] Knowledge of the $I = 0$ phase-shift solution above 550 MeV is less certain because of the fewer data available, the larger number of partial waves involved, and the greater importance of inelasticity.

Near 650 MeV, an extensively studied region, there exist significant discrepancies between published values of the n-p differential cross section, a basic observable. Results[3] obtained at the Princeton-Pennsylvania Accelerator (PPA) were in substantial disagreement with older Dubna data,[4] and a more recent Saclay experiment[5] yielded yet different values. In this paper the results of a precise measurement of the n-p differential cross section at 647.5 MeV in the $51° \leq \theta^* \leq 179°$ c.m. angular region are presented. This experiment was the

first step in a program of *n-p* scattering studies at the Clinton P. Anderson Meson Physics Facility (LAMPF) aimed at a determination of the *n-p* isoscalar interaction. The results presented here resolve the aforementioned discrepancies and provide a solid basis for phase-shift analyses near 650 MeV.

For reference, some of the more recent measurements of *n-p* differential cross sections in the medium energy region will be noted here. In a preliminary account of the present experiment, the data in the backward angle charge-exchange (CE) region were reported by Evans *et al.*[6,7]; additional measurements in the CE region made at LAMPF as a function of energy between 160 and 800 MeV were reported by Bonner *et al.*[8] Similar measurements in the CE region made at Schweizerisches Institut für Nuklearforschung (SIN) between 180 and 590 MeV by Hürster *et al.*[9] were in good agreement with the LAMPF measurements. In an experiment at PPA, Bersbach *et al.*[10] measured *n-p* forward angle differential cross sections in the region from 58 to 291 MeV, and from a LAMPF experiment Carlini *et al.*[11] reported forward angle *n-p* differential cross section measurements at 790 MeV. Very recently, Keeler *et al.*[12] measured complete *n-p* differential cross sections at TRIUMF, at six energies between 212 and 495 MeV. References to other experimental work may be found in the compilation of Bystricky and Lehar.[4]

The experimental method and details are described in Sec. II, and the data analysis in Sec. III. The results are presented and compared with those of other experiments in Sec. IV.

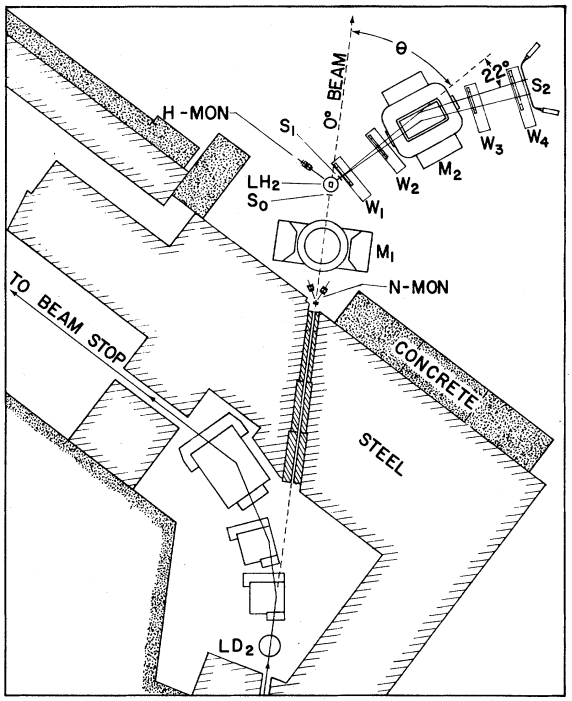

FIG. 1. Plan view of the experimental layout.

II. EXPERIMENTAL METHOD

Brief descriptions and some details of the methods and apparatus used in this experiment have been given in earlier publications.[6,13–15] A more thorough account will be presented here, and further details can be found elsewhere.[7] The experiment uses the LAMPF proton beam bombarding a liquid deuterium (LD_2) target to produce a nearly monoenergetic, collimated neutron beam at 0°, which impinges on a liquid-hydrogen (LH_2) target, as shown in Fig. 1. Individual charged particles ejected from the LH_2 target in a small angular region are detected in a multiwire proportional chamber (MWPC) spectrometer, which can be moved on an arc centered on the target. The spectrometer provides measurements of the scattering angles, momenta, and velocities of the particles. These data are used to distinguish between protons from *n-p* elastic scattering and deuterons from the $np \rightarrow d\pi^0$ reaction induced by neutrons from the monoenergetic peak of the neutron spectrum, as well as to separate these from charged particles produced in reactions induced by neutrons from the low-energy tail of the neutron spectrum, and from other charged particle backgrounds.

A. Neutron beam

The quality of the neutron beam used in *n-p* scattering experiments has a major influence on the accuracy of the results obtained. The LAMPF neutron beam used in this experiment was produced by proton bombardment of an LD_2 target and has a spectrum, shown in Fig. 2, which is characterized by a sharp, nearly monoenergetic charge-exchange peak ($\Delta E \simeq 12$ MeV FWHM) at essentially the proton beam energy, accompanied by a relatively small tail of lower energy neutrons attributable to reactions involving meson production and three-body breakup.[14] This beam is highly suitable for precise cross section measurements.

The neutron production target[16] contained LD_2 circulating under forced convection in a closed loop so as to eliminate the local boiling which would

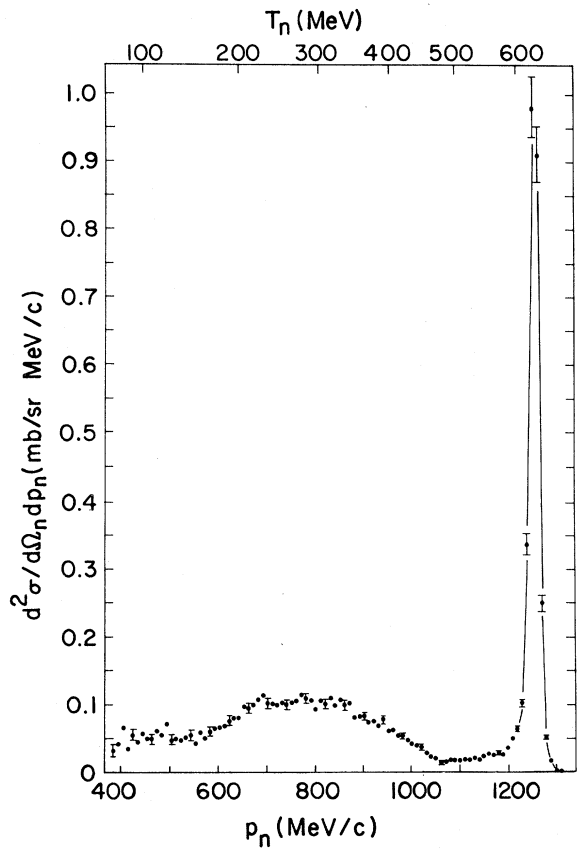

FIG. 2. Spectrum of the neutron beam incident on the LH_2 target.

otherwise occur due to beam heating with beam intensities of $\sim 1\ \mu$A. The LD_2 cooling was provided by a helium refrigerator of 200 W cooling capacity at ~ 14 K, with counter-current heat exchange between the cold helium gas and the circulating fluid. Electric heaters in the loop were used to regulate the LD_2 temperature. The beam entered and emerged from the target cell portion of the loop through curved aluminum windows of thickness 0.08 mm and area 13×2.5 cm^2. The thickness of LD_2 traversed by the beam was 10.8 cm; at a nominal liquid density of 0.163 g/cm^3 this gives a deuterium areal density of 5.3×10^{23}/cm^2. After leaving the target, the proton beam was deflected magnetically through an angle of 60° and buried in a beam dump. The LD_2 target region was enclosed in a thick shield wall made of steel and concrete. The collimator channel for neutrons produced at 0° was a circular hole of diameter 2.54 cm and length 3.66 m, formed by insertion of bored steel slugs into 155 mm gun barrel which penetrated the shield wall. The collimator exit was located 7.57 m from the center of the LD_2 target, thus defining a solid angle of 8.8 μsr (0.096° half-angle). A steel postcollimator of length 40.6 cm with a circular hole of a diameter 3.17 cm along the collimator axis was used to reduce the beam halo. Any residual charged particles in the beam were swept away by magnet M_1 placed between the collimator exit and the LH_2 target. The profile of the neutron beam at the location of the LH_2 target, as measured by the MWPC spectrometer, is shown in Fig. 3. The intensity of CE peak neutrons through the collimator was $\sim 8.7 \times 10^5/\mu$C of proton beam.[13]

B. Beam monitoring

The profile of the incident proton beam at the LD_2 target could be checked by insertion of a "harp" style wire scanner into the beam just upstream of the target. The beam was centered on the target (i.e., on the 0° collimator axis) typically within ± 0.5 mm both horizontally and vertically during the experiment, and its width and height were ~ 5 mm FWHM. The proton beam current was monitored by an inductive-pickup toroidal current monitor[17] located 5.18 m upstream of the target. The beam came in macropulses of frequency 120 Hz and duration 400 μs (5% duty factor). The toroid output which reflected this structure was amplified and sent to a signal processor, which removed a dc bias and 60 Hz noise pickup, and then to a current digitizer and scaler. The system was calibrated periodically by passing a calibrated current pulse, which duplicated the time macrostructure of the beam, into a wire loop through the toroid.

The neutron flux was monitored at the collimator exit by a pair of counter telescopes placed at horizontal scattering angles of 25° to the left and right

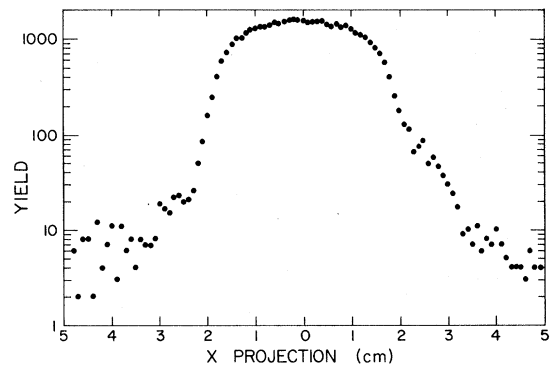

FIG. 3. Beam profile at the LH_2 target.

of the beam, which viewed a polyethylene radiator disk of diameter 3.17 cm and thickness 2.54 cm placed in the beam. Each telescope consisted of a pair of scintillators (Pilot U) of dimensions 7.6 cm×7.6 cm ×1.6 mm, separated by a copper absorber of thickness 4.57 cm, which made these telescopes relatively insensitive to protons with energies less than 210 MeV. A veto scintillator of thickness 1.6 mm placed just upstream of the radiator was used to reject events caused by stray charged particles in the neutron beam. This left-right flux monitor system, called N-MON, not only provided a reliable measurement of the relative neutron flux but also was sensitive to horizontal shifts of the neutron beam.

An additional monitor (H-MON in Fig. 1) was used to monitor the product of incident neutron flux and L H_2 target thickness. This monitor was a differential range telescope placed at 45° scattering angle, designed to be sensitive to protons coming from the region of the L H_2 target and having energies of 175—360 MeV (this brackets the energy expected for 45° proton recoils from 647 MeV *n-p* elastic scattering). This telescope consisted of scintillators H_1, H_2, and H_3, each 15.2 cm in height, 10.2 cm in width, and 1.6 mm in thickness (Pilot U), and veto scintillator H_4, which had dimensions 25.4 cm×15.2 cm×1.6 mm (Pilot U). Copper absorbers of thickness 3.43 and 3.81 cm were placed between H_2 and H_3, and H_3 and H_4, respectively. The angular acceptance of the telescope was determined by H_1, placed 40 cm from the L H_2 target, and H_3 placed 65 cm further away. Valid events were indicated by the coincidence pattern $\overline{H_1}\cdot H_2\cdot H_3\cdot H_4$. The counting rate in this monitor was ~11 times greater when the target was full than when it was empty.

C. Liquid-hydrogen target

The target flask was a cylinder of diameter 10.2 cm with rounded ends, hydroformed from 0.13 mm Mylar. It was oriented with its axis along the neutron beam axis; its length along the axis was ~13.2 cm when filled and under operating pressure, giving it an areal density of 0.94 g/cm^2 (5.6×10^{23} atoms/cm^2). It was enclosed in a radiation shield of aluminized Mylar and was contained within a vacuum chamber at 10^{-6} Torr, the outer wall of which was a cylindrical Mylar window of thickness 0.13 mm. Particles could emerge from the target with angles from 0° to 110° without obstruction. Refrigeration for the target was provided by a Cryodyne 1022 refrigeration system capable of extracting 5 W of heat from the target flask in the temperature range 15—24 K. Compensation for the excess cooling capacity was provided by an electric heater. This heater also could be used (with the H_2 supply valve closed) to drive the liquid hydrogen into a separate reservoir for the purpose of making background runs.

D. MWPC spectrometer

The primary detector in this experiment was the MWPC spectrometer. Since this instrument has been discussed in detail only in an unpublished report[18] it will be described at some length here. The elements of the MWPC spectrometer (see Fig. 1) were magnet M_2 which deflected charged particles ejected from the target, four multiwire proportional chambers W_1-W_4 which provided horizontal and vertical coordinate information at four points on each particle trajectory, and scintillators S_1 and S_2 which provided fast timing information. The spatial arrangment of these elements was rigidly maintained by a framework bolted to the magnet, which was also attached to a pivot mounted directly below the L H_2 target. The spectrometer could be rotated to any desired angle θ_{sp} with the aid of airpads under the magnet. Helium filled plastic bags with thin windows were placed in the spaces between the MWPC's in order to minimize multiple scattering of the particles.

1. Spectrometer magnet

Magnet M_2 was a "windowframe" type dipole magnet with rectangular polefaces of dimensions 91.44×45.72 cm^2 and a gap of 15.24 cm. At the highest current used (800 A) it could deflect an 800 MeV proton through an angle of 22°. Its magnetic field was mapped extensively using a rapid mapping device which measured all three components with an accuracy of 0.1% or better on a lattice of spacing 2.54 cm and overall dimensions 294.67 ×81.23×12.70 cm^3 at excitation currents of 200, 400, 600, and 800 A. These measurements were checked by nuclear magnetic resonance (NMR) probe measurements at the center of the gap and also by a long, narrow flip coil (dimensions: 320×1.92 cm^2) centered on the gap along its long dimension. These latter measurements determined the "bending power" $\int B_y dl$ along the central path of length 320 cm, where B_y is the vertical field component. All of these measurements were in

agreement within 0.1%. The measurements were made before the magnet was mounted on its support stand. The change in the field map at 200 A caused by presence of the stand was measured. The fractional changes in field at 400, 600, and 800 A were derived from the ratios of averaged values of the flipcoil measurements for the magnet on and off the stand. For any other current the correction was by interpolation based on flipcoil measurements at the current and at the above currents. It is estimated that the magnetic field was known during actual data runs with an overall accuracy of $\sim 0.7\%$.

2. Scintillators

The purpose of scintillator S_0 (see Fig. 1) was to veto any charged particles in the neutron beam. It was found later to have the effect of producing more unvetoed charged particles than were in the beam which struck it, and its use was discontinued. It did no real harm, however, because its contribution to the background was determined in the empty target runs.

Scintillator S_1 was placed ~ 15.3 cm downstream from the center of the LH_2 target. It was a square sheet of Pilot U of 231 cm^2 area and 0.8 mm thickness, supported inside a reflective tent (see Fig. 4) with walls consisting of one layer of aluminum foil of thickness 0.025 mm and three layers of aluminized Mylar of thickness 0.013 mm. The base of the tent was fixed to a Plexiglass light pipe, which in turn was glued to the face of an RCA 8575 photomultiplier tube. The use of the tent arrangement, which maximizes light collection efficiency, rather than an earlier version of S_1, which used only an adiabatic light pipe to couple the scintillator to the phototube, resulted in an improvement in pulse-height resolution from 150 to 60%.

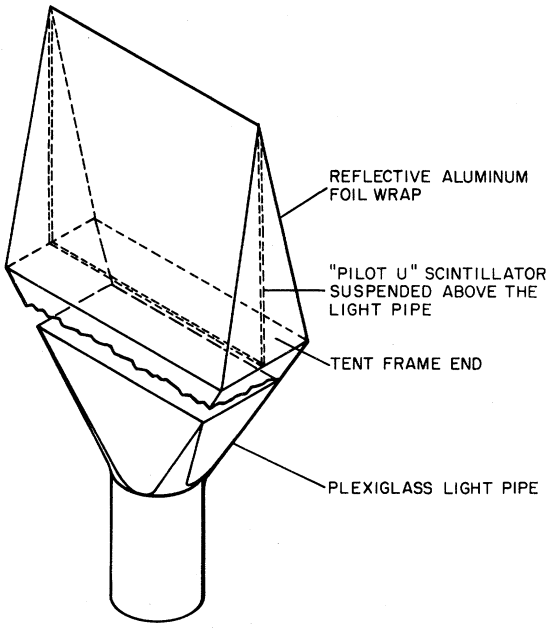

FIG. 4. Tent construction of the scintillator S_1 assembly.

Scintillator S_2 was placed 10.2 cm from the center of chamber W_4, which made the distance between S_1 and S_2 approximately 4.5 m. It was a sheet of Pilot F of width 101.6 cm, height 30.5 cm, and thickness 4.8 mm. It was viewed from both ends through curved adiabatic light guides by EMI 9813B photomultiplier tubes, called S_{2L} and S_{2R}. The light collection efficiency for either phototube was found to vary by a factor of 2 as a collimated ^{207}Bi beta source was moved across the width of the scintillator. In practice, the dynode outputs of the two phototubes were summed and the resultant pulse-height resolution was $\sim 60\%$. The time of flight t_{12} between S_1 and S_{2L} was used for particle identification. For a 650 MeV proton having an average trajectory, the time of flight resolution, after off-line correction for scintillator time walk, was 11% FWHM, easily sufficient for discrimination between protons, deuterons, and pions of the same momentum.

3. Wire chambers

The MWPC's were counters of the Charpak type[19] with sense-wire spacing of 2 mm and individual wire readout. Chambers W_1, W_2, and W_3 were of identical construction, while W_4 was similar but larger. Each chamber contained two signal planes, one with horizontal sense wires which gave vertical coordinate information, and another with vertical sense wires which gave horizontal coordinate information. Each signal plane was sandwiched between a pair of negative high-voltage wire planes having wires of 1 mm spacing and a direction perpendicular to that of the sense wires. The frame for each plane was made of G-10 fiberglass-epoxy laminate of thickness 4.7 mm (6.35 mm for W_4). The printed circuit boards for signal and high voltage connections were inlayed with epoxy in each frame. The wires were stretched, accurately positioned, and bonded into place with epoxy resin. The sense wires were made of gold-plated tungsten of 20 μm diameter, stretched with tension 0.5 N. The high-voltage wires were made of silver coated Cu-Be of 50 μm diameter stretched with tension 1.6 N. The sensitive area of chambers

$W_1 - W_3$ was 39.1 cm horizontal by 19.9 cm vertical, while that of W_4 was 64.7 cm horizontal by 39.1 cm vertical.

The separation between W_1 and W_2 and between W_3 and W_4 was 100 cm. With the sense-wire spacing of 2 mm the angle between the incident and emergent particle trajectories (i.e., the deflection angle) could be determined on the average with accuracy of ~ 2 mrad. Since a typical deflection angle was 22° (~ 380 mrad), it could be determined with an accuracy of $\sim 0.5\%$. The occurrence of multiple scattering and energy loss, primarily in the LH_2 target and in S_1, caused an additional uncertainty in the determination of the initial momentum and angle of the proton or deuteron, resulting in an effective spectrometer resolution of $\sim 1\%$ at 800 MeV.

Because of the detailed knowledge of the magnetic field, four x and four y coordinates provided an overdetermination of the particle trajectory, and in practice only three x and three y chamber signals were needed for an event to be considered valid. On the other hand, the chambers were capable of handling multiple hits, and events of considerable complexity were not rejected as long as both x and y signals from at least three of the four chambers were available. Another limit on the complexity of events will be noted in Sec. II E.

The counter-gas mixture used was (by volume) 56% argon, 37.9% isobutane, 0.1% freon 13B1, and 6.0% methylal and flowed continuously through the chambers. This mixture is similar to the CERN "magic gas"[20] but contains less argon and freon and more isobutane to compensate for the lower atmospheric pressure at LAMPF. The function of the methylal is to increase the effective lifetime of the chambers in high radiation fields.[21] It was introduced by bubbling the rest of the mixture through a reservoir maintained at -12 °C. With this mixture at an internal pressure of 0.79 atm (local atmospheric pressure) chambers $W_1 - W_3$ could be operated at 3.5–3.8 kV with detection efficiency per wire of 99.7%. The operating voltage for W_4 was ~ 4.2 kV for similar detection efficiency.

4. *Spectrometer acceptance*

The geometric acceptance of the spectrometer is a complicated function of the polar and azimuthal angles of scattering θ and ϕ, the momentum p, the magnet current, and the origin of the scattering (within the overlap of the neutron beam and the LH_2 target). Most of the complication arises because of the indefiniteness of the origin of the scattering. In order to exclude θ and ϕ angles which could lead to paths which strike the magnet poles and thus have a poorly known detection efficiency, it is necessary to require that the vertical component of the scattering be limited. With the spectrometer geometry and beam dimensions of the present experiment, this requirement is met if

$$|\sin\theta \sin\phi| \leq 0.02 .$$

Imposition of this requirement, however, means that for the cases in which $\sin\theta > 0.02$ only a fraction of the region of ϕ is accepted. Since the incident neutron beam is unpolarized, the azimuthal distribution is uniform and the fraction in effect becomes a geometrical detection efficiency and is given by

$$\epsilon(\theta) = \frac{2}{\pi}\sin^{-1}\left[\frac{0.02}{\sin\theta}\right]; \quad \sin\theta > 0.02 ,$$
$$\epsilon(\theta) = 1.0; \quad \sin\theta \leq 0.02 . \tag{1}$$

This efficiency function is shown in Fig. 5.

It is convenient at this point to define three coordinate frames of reference, all being right-handed and having y axes pointing upward. The laboratory frame (x_l, y_l, z_l) is centered in the LH_2 target with its z axis in the beam direction. The magnet frame (x_m, y_m, z_m) is fixed in the magnet with its origin at the center of the magnet gap and its z axis pointing downstream parallel to the magnet's long dimension. (The magnet frame and other geometric factors involved in the momentum analysis are shown in Fig. 11.) The spectrometer frame (x_s, y_s, z_s) is also fixed relative to the magnet, but its origin is at the center of the LH_2 target and its z axis points to-

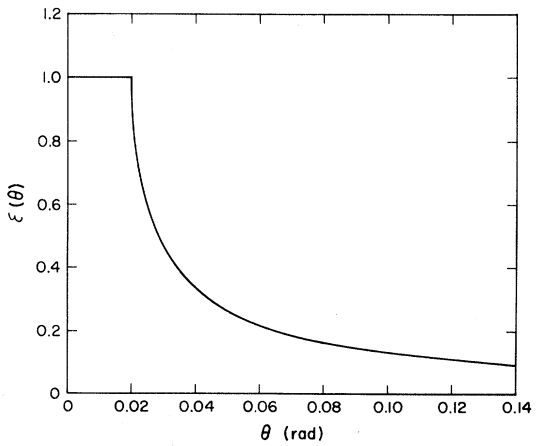

FIG. 5. Limit on the geometric acceptance of the spectrometer imposed by the magnet polefaces.

ward the spectrometer, perpendicular to planes W_1 and W_2.

The polar and azimuthal angles in the spectrometer system are θ_s and ϕ_s. In order to be certain that particles are being detected with the above efficiency it is necessary in addition to restrict θ_s to values such that the particle orbits miss none of the wire planes. This restriction was determined empirically from the spectrometer data in the off-line analysis (see Sec. III B) by generating computer plots of θ_s vs hit-wire position for all eight wire planes, and for a series of momentum bands for each magnet current. An example of such plots is shown in Fig. 6, which displays θ_s vs W_3x and W_4x, the horizontal coordinates of hits in W_3 and W_4, respectively, for a magnet current of 600 A and a momentum band $1200 < p < 1250$ MeV/c. Note that the left edges of the plots correspond to right scatterings in the magnet frame. It is clear from the plots that no particles in this momentum band are missing W_4 but some of those with $\theta_s > 30$ mrad are beyond the edge of W_3. It is also clear, however, that particles scattered to the right with angles $\theta_s < 30$ mrad are hitting both planes. Similarly, by inspection of the right edges of the plots it can be seen that particles scattered to the left in the magnet frame with angles $\theta_s < 50$ mrad would hit both planes, while some particles scattered to the left with $\theta_s > 50$ mrad would be beyond the edge of W_3. By inspection of a large number of plots such as these it is possible to determine a "safe" region of θ_s, in which all particles have orbits which pass through all of the wire planes.

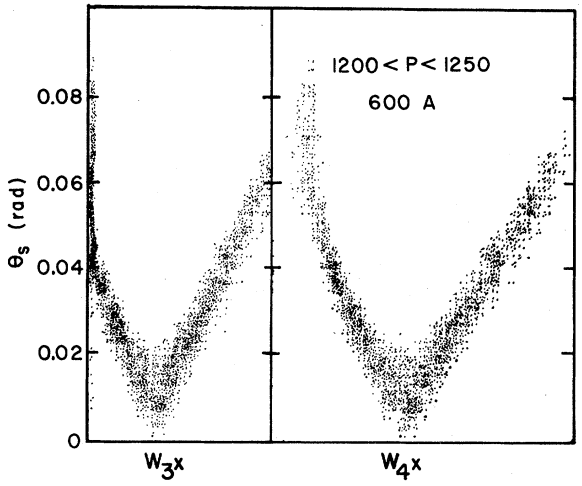

FIG. 6. Empirical plots of θ_s vs W_3x and W_4x obtained with 600 A magnet current for a selected momentum band.

This information, summarized in Fig. 7, shows the left and right limits of θ_s plotted versus the momentum (divided by magnet line integral for each magnet current). The area from upper left to lower right between the loci of plotted points is a region in spectrometer phase space within which a particle passes through all wire planes. For the purpose of computer analysis the safe acceptance region was parametrized as shown by the polygon in Fig. 7; the geometrical efficiency for particles in this region is given by Eq. (1).

5. *MWPC electronics*

The objective of the wire-chamber electronics was to determine which sense wires were hit within a time window generated by a master gate, and in case of a valid event to provide a coded 16 bit word which identified the plane and the wires which were hit. Details of this system have been given by Werren *et al.*[18]; a brief summary is given here. The signals from each group of eight neighboring wires (called a module) were processed by an amplifier/logic card which plugged into the printed circuit board on the sense-wire plane. These cards had an amplifier, a discriminator, and a monostable pulse generator for each of the eight wires in a module. When a wire was hit the corresponding monostable circuit would be activated, generating pulse of length ~ 680 ns. Thus a pattern of hit wires produced by an event was retained for this period as a pattern of monostable pulses. Meanwhile, each activated module would also send a fast signal to remotely located electronics for use

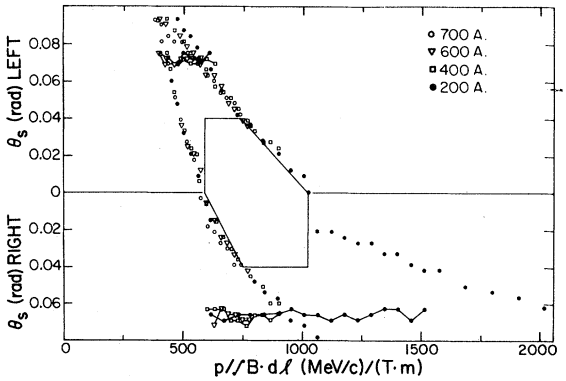

FIG. 7. Plot of θ_s vs momentum, showing the empirically determined limits on the geometric acceptance of the spectrometer imposed by the edges of the wire planes. Division of p by $\int B \cdot dl$ removes the dependence on magnet current.

in the decision-making logic. If the criteria for a valid event were met, a write-gate pulse of length ~80 ns was sent back to the modules, and if the write gate overlapped the trailing edge of the 680 ns monostable pulse (or pulses), this overlap would generate appropriate signals on eight output lines, one for each wire, specifying the hit pattern. It would also send a signal indicating that the module was "active" to an encoder which would construct another eight bits of binary coding, three of which specified the location of the module within a supermodule (group of eight modules), three bits to give the location of the supermodule within a chamber, and two bits to identify the chamber. The 16 bit data word for each active module was put onto the data bus leading to the scratch pad memory (SPM) in an order determined by a priority encoding system, and then the module was reset. The SPM is a fast intermediate buffer, designed by Brown,[22] which read and stored the MWPC data while such things as ADC and TDC conversion took place.

The summed outputs of the monostable pulses for each plane gave an analog measure of the number of wires hit in that plane, which was useful for diagnostic purposes.

E. Data acquisition electronics

A block diagram of the data acquistion system is shown in Fig. 8. The trigger signal for valid events was provided by the block labeled NIM, which is shown in more detail in Fig. 9. The requirement to be met was a coincidence (within 50 ns) between signals from scintillators S_1 and S_2 along with $\frac{3}{4}$ majority coincidences with the fast discriminator signals from both the horizontal and vertical wire planes of the four MWPC's, all in the absence of a veto signal from scintillator S_0. This requirement can be abbreviated:

$$(\overline{S_0}\cdot S_1\cdot S_2)\cdot(W_1x\cdot W_2x\cdot W_3x\cdot W_4x)_{3/4}\cdot(W_1y\cdot W_2y\cdot W_3y\cdot W_4y)_{3/4}\ .$$

The timing of the master gate output was dominated by the time of the signal from S_1. When the master gate detected a valid event its output set an inhibit which blocked further triggering until the data from that event had been stored, started the time-to-digital converter (TDC), opened the fast linear gates, strobed the analog-to-digital converters (ADC's), formed the write-gate pulse which generated the hit-pattern outputs from the MWPC's, and went to the SPM, which sent an encode enable signal to the MWPC's initiating the readout of the MWPC data to the SPM.

A further measure taken to speed up the data-acquistion process was the use of a microprogrammed branch driver (MBD),[23] a device which is capable of buffering incoming data during the beam macropulse and transferring the data to the PDP-11/20 computer between macropulses. In this way several events per macropulse could be obtained.

While the ADC and TDC conversion and readings were taking place, the encode enable signal went to the MWPC's and by a predetermined priority system enabled for each active module the encoding of the 16 bit MWPC word discussed in Sec. II D 5, the sending of the word *via* the data bus to the SPM, and the resetting of the module. As each module was reset the encode enable signal was sent to the remaining active module of highest priority and the process was repeated until all active modules had been read or the number of MWPC words exceeded 15. If the latter had occurred the event was rejected by the MBD.

When all ADC and TDC conversions were completed a signal was sent to the priority interrupt register which told the MBD that the event was ready to be read. The MBD read the analog information contained in the octal scalers, packing two ADC's per 16 bit word and buffering it in its own memory.

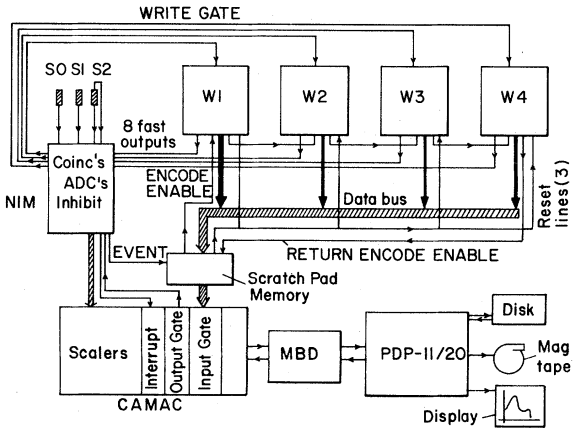

FIG. 8. Simplified block diagram of the data acquisition electronics.

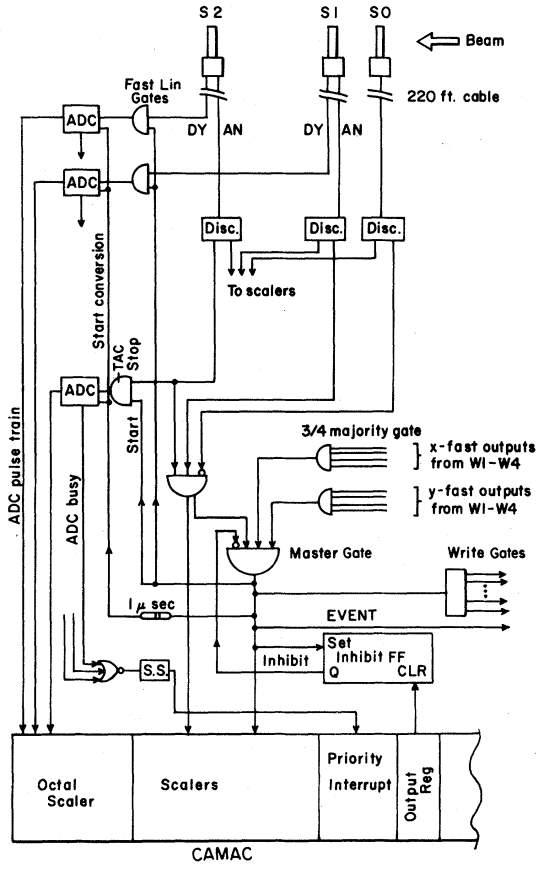

FIG. 9. Diagram showing the logic used to identify valid events and generate the gates needed to process them.

The SPM was then interrogated and when all of the MWPC words had been read into the SPM, the contents of the SPM were read into the MBD memory through a specially designed CAMAC input gate, the inhibit was ended, and the system was ready to receive the next event.

F. Data acquisition program

The on-line data acquistion was controlled by a computer program DAISY (Ref. 24) which buffered the data coming from the MBD, wrote the data on magnetic tape for later off-line analysis, and in the case of "perfect" events (those having only one hit wire registered in each of the eight wire planes) generated a variety of histograms and two-parameter plots which were stored on a rotating disk and made available for run-time display and diagnostic purposes. Two examples of particular interest are shown in Fig. 10. The first, shown in Fig. 10(a), is

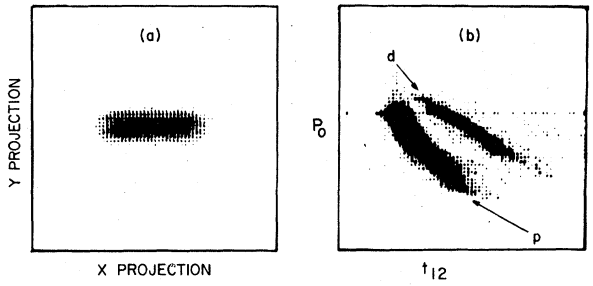

FIG. 10. Samples of two-dimensional density plots provided on-line by the data acquisition program. (a) Projection of the particle incident path in the spectrometer onto the midplane of the LH_2 target. The horizontal elongation shows the finite length of the target when viewed from a large angle setting of the spectrometer. (b) Plot of the approximate particle momentum p_0 (given by the magnetic deflection angle) vs time of flight between scintillators S_1 and S_2, showing the clear separation of protons (indicated by p) and deuterons (indicated by d).

the "target projection," i.e., the horizontal and vertical coordinates of the scatterings in the LH_2 target as inferred from the hits registered in W_1 and W_2. The elongation in the horizontal direction arises from the fact that the spectrometer was set at a large angle and reflects the finite length of the LH_2 target. The display shown in Fig. 10(b) is a plot of the approximate momentum p_0 (estimated from the angle of magnetic deflection) vs t_{12}, the time of flight through the spectrometer, and shows how protons can be distinguished from deuterons of the same momentum.

G. Data taking procedure

The data were obtained in two sets of runs, some six months apart, in which different methods were used to vary the scattering angle accepted by the spectrometer. In the first set the spectrometer was positioned at 0°, and data of high statistical accuracy ($\sim$200 000 master gates) were obtained for each of three different magnet currents. As the current was lowered, the θ_s-acceptance region of the spectrometer shifted to larger θ_s values, providing data on $d\sigma/d\Omega^*$ for $174.5 < \theta^* < 180°$. In the second set of runs the spectrometer position was changed in 4° steps from 0° to 60°. The magnetic field of the spectrometer was decreased as the angle increased, to match the decreasing momentum of the scattered protons. The number of master gates obtained at each angle varied from $\sim$200 000 at 0° to $\sim$38 000 at each of the seven largest angles, to some degree

reflecting the variation of $d\sigma/d\Omega^*$. For each run obtained with the LH_2 target filled, a background run was obtained with the target cell emptied. The number of master gates obtained for each empty-target run was typically $\sim 3\%$ of the number obtained with full-target runs; the time spent on background runs was $\sim 30\%$ of the total data acquisition time.

H. Normalization

Relative normalization of individual runs was provided by both the toroidal proton-beam monitor and the left-right neutron-beam monitor, N-MON, which were consistent within 1.6%. For target-full runs, the ratio of the number of counts in N-MON and in H-MON remained constant within 1.1% (essentially the statistical accuracy of the H-MON count), which indicated constancy of the LH_2 target thickness. The N-MON count was used for the relative normalization of runs since it was proportional to the integrated neutron flux for both full and empty targets. It was recorded by a scaler which was gated off by the spectrometer (master gate) inhibit, so as to make a deadtime correction unnecessary. The deadtime could be measured, however, by comparing the gated N-MON count with the N-MON count recorded by an ungated scaler. Typical deadtimes were 20% for target-full runs and 2% for target-empty runs.

For spectrometer angles up to 13°, deuterons from the reaction $np \rightarrow d\pi^0$ were detected along with the protons from n-p elastic scattering. Since the cross section for the $pp \rightarrow d\pi^+$ reaction is reasonably well known ($\sim 5\%$ accuracy[25]), and by isospin conservation is expected to be twice the cross section for $np \rightarrow d\pi^0$, the yield of deuterons can be used to determine the product $N_t N_n$, where N_t is the number of target hydrogen atoms per cm^2 and N_n is the number of incident neutrons passing through the target during a run. The estimated overall accuracy of this determination of $N_t N_n$ is $\sim 7\%$.[26] This provided absolute calibration of N-MON with 7% accuracy. This calibration technique is discussed in more detail in Sec. III B 4.

I. Angular uncertainty

The uncertainties in laboratory scattering angle arose from multiple scattering in the LH_2 target and scintillator S_1 ($\pm 0.10°$ at $\sim 0°$ to $\pm 0.45°$ at $\sim 60°$), from multiple scattering and geometrical resolution effects within the spectrometer ($\pm 0.08°$ at $\sim 0°$ to $\pm 0.24°$ at $\sim 60°$), and from uncertainties in the spectrometer position and the MWPC alignment ($\pm 0.10°$). Combined in quadrature these give overall uncertainties in laboratory angle ranging from $\pm 0.16°$ at $\sim 0°$ to $\pm 0.52°$ at $\sim 60°$. The corresponding errors in θ^* range from $\pm 0.27°$ at $\sim 180°$ to $\pm 0.97°$ at $\sim 50°$.

III. DATA REDUCTION AND ANALYSIS

There were two stages in the analysis, involving two FORTRAN programs, KIOWA[27] and TEWA. The function of TEWA was to read the raw data tape generated by DAISY, to apply preliminary cuts to the data, to calculate p, θ_s, and ϕ_s, and to write these and a number of other parameters for the event onto an intermediate tape. The program KIOWA was used to read this tape, apply various corrections to the data, impose final cuts, separate deuterons from protons, sort the events of interest into a variety of histograms and two-dimensional plots, and calculate the cross section values.

A. TEWA

The most critical and time-consuming job done by TEWA was that of determining the momentum of the particle in an event from the MWPC hit positions and the magnetic field map. Since this took, on the average, 12 ms of CDC 7600 computer time per analyzed event, it was important not to process unuseful and grossly defective events. An example of the latter is an event in which a cluster of more than seven adjacent wires all registered hits. Less severely defective events could be treated, but the discussion of that treatment will be deferred (see Secs. III A 2 and III A 3).

1. Perfect events

By a perfect event is meant one in which a single hit or cluster is registered in each of the eight wire planes (this was the case for $\sim 90\%$ of the events.) If a cluster is observed its center is taken as the hit position. With perfect events the angle of magnetic deflection α is easily determined, and from this an approximate value p_0 for the momentum of the particle is given by

$$p_0=\frac{k}{\alpha}\int B_y\,|\,d\vec{l}\,|\ ,$$

where k is a constant, B_y is the vertical component of the magnetic field $\vec{B}$, $d\vec{l}$ is a line element along the trajectory, and the value of

$$\int B_y\,|\,d\vec{l}\,|$$

is that determined for a typical path at each magnet current. The equation of motion of the particle, derived from the Lorentz equation, is

$$\frac{d^2\vec{r}}{dl^2}=\frac{e}{p}\hat{u}\times\vec{B}\ , \tag{2}$$

where $\vec{r}$ is the position vector of the particle, $\hat{u}=\vec{v}/|v|$ is a unit vector along the line element $d\vec{l}$, and e and p are the charge and momentum of the particle, respectively. The numerical integration of this equation is done in the magnet reference frame, shown in Fig. 11. Since the largest and most important deflection component was the horizontal, attention will be focused on that. The initial coordinates x^i and z^i and slope $(dx/dz)^i$ of the trajectory as it crossed the "start plane" (i.e., the midplane between W_1 and W_2) were determined from the hit wires of W_1 and W_2. The calculated slope $(dx/dz)^*$ and coordinate x^* of the trajectory where it intersected the "end plane" (i.e., the midplane between W_3 and W_4) were then determined for a particle of momentum p_0 by numerical integration of the x component of Eq. (2) through the spectrometer, making use of the stored magnetic field map. The results are

$$\left[\frac{dx}{dz}\right]^*=\left[\frac{dx}{dz}\right]^i+\frac{e}{p_0}I_i^*\left[\frac{dl}{dz}\right]^* \tag{3}$$

and

$$x^*=x^i+(z^*-z^i)\left[\frac{dx}{dz}\right]^i+\frac{e}{p_0}I_2^*\ , \tag{4}$$

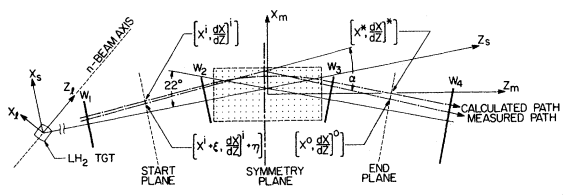

FIG. 11. Schematic diagram of the spectrometer geometry, showing the relationships between coordinate systems and also identifying some measured quantities and some of those calculated in the analysis.

where

$$I_1^*=\int_0^l(\hat{u}\times\vec{B})_x dl \tag{5}$$

and

$$I_2^*=\int_0^l dl\int_0^l(\hat{u}\times\vec{B})_x dl-\left[\frac{dx}{dz}\right]^i\times\int_0^l dl\int_0^l(\hat{u}\times\vec{B})_z dl\ . \tag{6}$$

The only approximation made in arriving at the above is that

$$\left[\frac{dz}{dl}\right]^i=\left[\frac{dz}{dl}\right]^*\ ,$$

which generally is true to better than 1%. In general, the measured slope $(dx/dz)^o$ and coordinate x^o will differ from the calculated values $(dx/dz)^*$ and x^*. If it is assumed that the initial coordinate x^i and slope $(dx/dz)^i$ are in error by amounts ξ and η, respectively, and that the true momentum p and the estimate p_0 are related by the formula

$$1/p=\rho+(1/p_0)\ ,$$

then the statistical function χ^2 which measures the goodness of agreement between the measured and true values of the coordinate and slope at the start plane and at the end plane is

$$\chi^2=\frac{\xi^2}{\sigma_1^2}+\frac{\eta^2}{\sigma_2^2}+\frac{1}{\sigma_3^2}\times[x^*+\xi+(z^*-z^i)\eta+\rho eI_2^*-x^o]^2+\frac{1}{\sigma_4^2}\left[\left[\frac{dx}{dz}\right]^*+\eta+\rho e\left[\frac{dl}{dz}\right]^*I_1^*-\left[\frac{dx}{dz}\right]^o\right]^2\ , \tag{7}$$

where the standard deviations σ_i are estimates based on wire-plane resolution, cluster size, and multiple scattering effects. The terms in the first pair of square brackets are the differences between the "true" and measured coordinates at the end plane while those in the second are the differences between the true and measured slopes at the end plane. Minimization of χ^2 was achieved by setting the derivatives $\partial\chi^2/\partial\rho$, $\partial\chi^2/\partial\xi$, and $\partial\chi^2/\partial\eta$ equal to zero and solving the resultant simultaneous equations for ρ, ξ, and η. These corrections could be used to generate new starting values for an iteration of the procedure, but experience showed that a single iteration was sufficient to yield a momentum

value correct to within 0.5%. Similarly, it was found by experience that χ^2 minimization for the vertical motion was unnecessary.

2. *Missing coordinates*

Events could be analyzed if no more than one x and one y coordinate were missing. From an investigation of perfect events it was determined that straight-line projections of the incident and final trajectories came close to intersection at a plane called the "symmetry plane" of the magnet (see Fig. 11). The location of this plane varied with the magnet current but was never far from $z=-1.0$ cm and was reasonably well determined. This fact made it possible to supply a value for the missing coordinate when, because of inefficiency or a defective wire, one of the wire planes failed to register a hit. This was done by finding the intersection of the well-determined projection given by two of the coordinates with the symmetry plane, and then constructing a straight line between that point and the third available coordinate. The intersection of this line with the missing plane provided the missing coordinate.

3. *Multiple clusters*

Events containing up to 15 wire-plane hits were accepted by the data-acquisition system. These could arise from accidental coincidences between real events and noise pulses or ambient background pulses, or could be caused by two real particles traversing the spectrometer. The case when only one x and/or y plane had multiple hits was handled easily by treating the coordinates of the planes involved as missing coordinates. More complex hit patterns were handled by considering all possible combinations, doing the numerical integration for each in turn and keeping the two solutions having the smallest value of χ^2. The information on both of these was written onto the intermediate tape.

4. *Output*

After reconstruction of the event and minimization of χ^2, TEWA wrote all available information on the event onto the intermediate tape. This included the calculated momentum and χ^2, t_{12}, pulse heights in S_1 and S_2, hit-wire positions, scattering angles, magnetic deflection angles, path length l, projections to the symmetry plane of the LH_2 target, and other calculated quantities. At the end of each run, all of the scaler information for the run was also written onto this tape.

B. Code KIOWA

The code KIOWA was basically a histogramming and plotting code, modified to perform several other functions as well. It read the intermediate tape generated by TEWA and, event by event, applied various cuts and corrections before incrementing a wide variety of histograms and two-dimensional arrays. It determined, for example, whether the event fell in the safe region of Fig. 7, made the coordinate transformation from the spectrometer reference frame to the n-p scattering (laboratory) reference frame and corrected t_{12} for the discriminator time walk in the signals from S_1 and S_2 and for the dependence of the S_2 timing on the position of the event within the scintillator. In addition, identification of the particle mass and a compensation for MWPC granularity effects were made, as will be discussed in more detail below. Finally, from the observed particle momentum and angle, appropriate kinematic relationships were used, for protons and deuterons separately, to determine the incident neutron energy on the assumption that elastic scattering (or the $np \rightarrow d\pi^0$ reaction) had taken place. In this way, a reconstructed incident neutron energy spectrum could be obtained.

When all of the events in a run had been read and stored in appropriate arrays, these arrays were printed out and the cross section values were calculated. The analysis of the data using KIOWA always involved at least two passes, and usually several more. The preliminary passes were made with relatively loose cuts and were primarily diagnostic runs, in which placements of final cuts were determined.

1. *Particle identification*

It was seen in Fig. 10(b) how mass identification of the particle can be made from a plot of p vs t_{12}. Unfortunately, the separation of protons from deuterons on such plots was less than perfect because accidental coincidences between real events and background sometimes caused an erroneous value of t_{12}. Therefore, some of the events on the deuteron side of the cut on that plot were actually proton events. These were identified by placing a narrow window about the momentum expected for n-p elas-

tic scattering and plotting the pulse height observed in S_2 vs t_{12} for events which fell on the deuteron side of the p vs t_{12} cut. Since protons and deuterons of the same momentum gave different pulse heights, it was easy to distinguish true deuterons from protons which had been mistakenly identified by the p vs t_{12} cut.

2. MWPC granularity

The discreteness of the coordinate information provided by the MWPC's caused artificial irregularities to appear in the angular distributions. The cause of this problem was the incompatibility between the lattice of rectangular coordinates in which the scattering angle of the particle was measured and the spherical coordinate system in which the events were binned. In the limit of very small wire spacing, of course, the effect becomes negligible, but with the 2 mm wire spacing in the MWPC's it was significant. The problem was made worse in some regions of W_1 and W_2 by the fact that two or three neighboring wires became short-circuited to each other, resulting in an effective wire spacing of 4 to 6 mm. The solution adopted was to randomize the discrete coordinates of W_1 and W_2 into trapezoidal distributions about the discrete values, having widths comparable to the wire spacing (or the width of the group in the case of shorted wires), before calculating the scattering angles. Further details are given in Ref. 7.

3. Neutron spectrum and momentum window

Because the uncertainties caused by multiple scattering and energy loss were smallest in runs with the spectrometer at 0° in the laboratory frame, the neutron spectrum reconstructed by KIOWA from recoil proton data in the 0° runs gave the most accurate determination of the incident neutron beam spectrum (Fig. 2).

One objective in the analysis was to ensure that only events produced by neutrons from the high-energy CE peak in the spectrum were used in the cross section determination. This was true both for the protons from n-p elastic scattering and for the deuterons from the $np \rightarrow d\pi^0$ reaction. The placement of a window on the peak in the reconstructed neutron spectrum was complicated by the effects of multiple scattering and energy loss, which broadened and shifted this peak as the spectrometer was moved to larger angles. For each spectrometer setting, the window was placed to enclose the CE peak of this reconstructed spectrum without including too much contribution from regions outside the peak. This somewhat arbitrary procedure became less certain as the effects of energy loss and multiple scattering increased. A further consequence of these effects was to shift some particles out of the CE peak into the reconstructed valley and vice versa. Optimum placement of the window would be achieved if the numbers crossing out of and into the window were balanced. A correction for imperfect placement of this window will be discussed in Sec. III C 2.

4. Cross section calculation

Background runs made with the $L H_2$ target empty were treated in exactly the same way as target-full runs. Full-target runs at a common spectrometer setting were simply added together, and empty-target runs, normalized to the same gated N-MON count, were subtracted. The summed data were then sorted into θ bins of width 5.5 mrad, all falling entirely within the safe region of the spectrometer acceptance (Fig. 7). The same procedure was followed separately for protons and deuterons.

The yield of protons in the nth θ bin ($\theta_1 < \theta < \theta_2$) with mean angle $\overline{\theta_n}$ is given by

$$(Y_p)_n = N_t N_n \frac{d\sigma(\overline{\theta_n})}{d\Omega} 2\pi(\cos\theta_1 - \cos\theta_2)\epsilon(\overline{\theta_n}) , \tag{8}$$

where $d\sigma(\overline{\theta_n})/d\Omega$ is the n-p differential cross section (laboratory) and $\epsilon(\overline{\theta_n})$ is the geometrical efficiency factor (Fig. 5). Similarly, the yield of deuterons in the mth θ bin (corresponding to $\theta_i^* < \theta^* < \theta_2^*$ in the c.m. system) with mean angle $\overline{\theta_m}$ (laboratory) is given by

$$(Y_d)_m = N_t N_n \epsilon(\overline{\theta_m}) \int_{\theta_1^*}^{\theta_2^*} \frac{d\sigma}{d\Omega^*} d\Omega^* , \tag{9}$$

where $d\sigma/d\Omega^*$ is the c.m. differential cross section for the $np \rightarrow d\pi^0$ reaction, presumed to be one-half the cross section for $pp \rightarrow d\pi^+$. Since this cross section is known, Eq. (9) can be solved for $N_t N_n$, thus determining the proportionality between the N-MON count and $N_t N_n$, and in effect calibrating N-MON.

Actually, what was done was to start with the existing parametrizations[25] of the total and differential cross sections for $pp \rightarrow d\pi^+$ and to account for the mass difference between that and the $np \rightarrow d\pi^0$ reaction by assuming the cross sections to be the

same (except for the factor of 2 from isospin conservation) at the same deuteron c.m. momentum. The proton energy in $pp \rightarrow d\pi^+$ corresponding to the mean neutron energy in the present experiment (647.5 MeV) was 655.4 MeV, at which the total cross section for $pp \rightarrow d\pi^+$ was taken to be 2.86 mb. In accord with the usual procedure[25] the c.m. differential cross section was assumed to have the functional form

$$\frac{d\sigma}{d\Omega^*} \propto A + \cos^2\theta^* + B\cos^4\theta^* , \tag{10}$$

with provisional values of A and B as given in Ref. 25. The present deuteron data were then analyzed to determine the relative angular distribution for the $np \rightarrow d\pi^0$ reaction, and the results were least-squares fitted with Eq. (10), providing a new determination of A and B.[28] These values ($A=0.235$; $B=-0.411$) were then used in a final determination (with statistical accuracy $\sim 1\%$) of the N-MON calibration in terms of $N_t N_n$ using all of the deuteron data. With $N_t N_n$ determined, the n-p differential cross section values could be calculated from Eq. (8). It is appropriate to note here that if a future determination of σ_n (647.5), the total cross section for the $np \rightarrow d\pi^0$ reaction at 647.5 MeV, leads to a better value than 1.43 mb, then the n-p differential cross section values presented in this paper can be corrected accordingly through multiplication by the factor σ_n (647.5)/1.43 mb

The statistical error for the nth θ bin at a given spectrometer setting was calculated using the formula

$$\sigma_n = [(\sigma_f)_n^2 + C^2(\sigma_e)_n^2]^{1/2} / \{2\pi N_t N_n \epsilon(\overline{\theta_n})(\cos\theta_1 - \cos\theta_2)\} , \tag{11}$$

where $(\sigma_f)_n$ and $(\sigma_e)_n$ are the standard deviations for the nth bin of the target-full and target-empty runs, respectively, C is the normalization factor applied to the target-empty runs, and the value of $N_t N_n$ is that calculated for the target-full run.

C. Other corrections

No correction was needed for deuterons coming from the reaction $n + p \rightarrow \gamma + d$ because the window imposed on the reconstructed incident neutron energy spectrum was narrow enough to exclude such deuterons from the momentum region where the $d\pi^0$ deuterons were found. The cross sections for other inelastic reactions are small and involve three-body final states, and therefore contributed very few events to the tightly constrained kinematic regions where the two-body reactions were found. Another source of error was the elastic p-p scattering of the recoil protons, primarily within the LH_2 target. Such protons could be scattered into or out of the spectrometer acceptance region. Since the yield loss from this effect was estimated to be quite small ($<0.5\%$) and the outscattering was compensated to some extent by inscattering, no correction was made. Two types of additional corrections, were made, however.

1. Absorption corrections

The probability of a recoil proton being absorbed while emerging from the LH_2 target or passing through elements of the spectrometer was estimated from the amount and nature ($\sim 95\%$ hydrogen) of the material traversed, using available data on p-p inelastic cross sections. The correction ranged from zero for protons with energies below the threshold for pion production to $\sim 0.5\%$ at the highest proton energies. A similar correction for outgoing deuteron absorption was determined through an attenuation calculation using the d-p total cross section as given numerically by the spline fit of Seagrave.[29] The correction varied smoothly from 1.7 to 2.0% as the deuteron momentum changed from 1400 to 1200 MeV/c.

2. Window corrections

The location and width of the window placed on the CE peak of the reconstructed neutron spectrum were important factors in the experiment. Ideally, only events caused by neutrons from within a corresponding CE window in the incident neutron spectrum would be used in the analysis. Actually, because of indeterminate energy and angle changes caused by energy loss and multiple scattering in the target and spectrometer, a certain number N_{iO} of the events initiated by neutrons within the CE window of the incident neutron spectrum fell outside the window (called the KIOWA window) placed on the neutron spectrum reconstructed by KIOWA. Similarly, of the events initiated by neutrons of energy outside the CE window, a certain number N_{Oi} fell inside the KIOWA window on the reconstructed

neutron spectrum. If N_{ii} is the number of events caused by neutrons of energy within the CE window which fell within the KIOWA window after event reconstruction, then the number of events which fell within the KIOWA window and were tallied was $N_{ii}+N_{Oi}$, while the number which should have been tallied was $N_{ii}+N_{iO}$.

These experimentally unobservable numbers were determined through use of a Monte Carlo calculation which simulated the n-p scattering experiment as accurately as possible. For each simulated event, a neutron of energy chosen randomly from a probability distribution approximating the incident neutron energy spectrum was made to undergo CE scattering at a point in the LH_2 target chosen randomly from a distribution reflecting the spatial profile of the neutron beam in the target. A random scattering angle in the range $0°-63°$ (laboratory) was chosen, and the momentum and kinetic energy of the recoil proton were calculated. The energy was corrected for energy losses in the target and spectrometer, and the recoil proton angle was changed by an amount randomly chosen from a probability distribution which approximated the multiple scattering distribution. Starting with the altered angle and energy, the simulated event then was processed in exactly the same way as a real experimental event was processed by KIOWA, i.e., n-p kinematics was used to calculate the incident neutron energy, and it was determined whether or not the event fell within the KIOWA window used in the analysis of real data at the appropriate spectrometer setting.

The results of such a calculation for 400 000 neutrons gave a distribution of events which simulated that which was observed in the experiment. These events were grouped into 4° angle bins corresponding to the spectrometer settings used in the experiment, giving $\sim$20 000 events for each setting. In the process, the unobservable numbers N_{ii}, N_{iO}, and N_{Oi} were determined for each spectrometer setting.

This Monte Carlo calculation was used first to determine the optimum placement of the CE window on the reconstructed neutron spectrum for the 0° spectrometer setting, i.e., the best available determination of the true incident neutron spectrum. For this calculation the CE window on the incident neutron spectrum and the KIOWA window on the reconstructed neutron spectrum for 0° spectrometer setting were taken to be the same, and the calculation was repeated with window adjustments until N_{iO} and N_{Oi} were both small and equal for the 0° spectrometer setting; for the other spectrometer settings the KIOWA windows were the same as those used in KIOWA. At this point, small differences between the centroids of the CE peaks in the spectra produced by KIOWA and those produced by the Monte Carlo simulation were noted. The KIOWA windows used in the simulation were then displaced to compensate for these differences, preserving their widths, and the calculation was repeated once more. From the results of this final calculation the window correction factor

$$(N_{ii}+N_{iO})/(N_{ii}+N_{Oi})$$

was determined for each spectrometer setting.

The cross section values produced by KIOWA were multiplied by these factors, correcting for imperfect window placement. The corrections were generally small at small spectrometer angle settings but became as large as 4% at some of the larger angles. The fractional accuracy of the corrections is estimated to be 10%. Such corrections were not needed for deuterons because their momenta were always so high that energy loss and multiple scattering effects were unimportant.

IV. RESULTS AND DISCUSSION

A. Results

As was noted earlier, the data were obtained in two sets of runs some six months apart. The first set covered only a small angular range at back angles ($174.5° < \theta^* < 180°$) and was obtained with a neutron beam of somewhat lower energy (632 MeV) than the second (647.5 MeV). The variation of $d\sigma/d\Omega^*$ with angle was virtually identical in the two data sets, and their absolute normalization differed by less than 1% (well within the statistical uncertainties involved). Since the elastic cross section varies only slowly with energy in this energy region the results for the two data sets were simply averaged, and because the second data set was much more comprehensive the energy quoted for the final results is 647.5 MeV.

The final center of mass differential cross section values are presented in the form $d\sigma/d\Omega^*$ in Table I, as well as in the alternative form $d\sigma/du$ (where $-u$ is the square of the neutron four-momentum transfer), along with the corresponding center of mass angles θ^*. The errors quoted are those calculated using Eq. (11) and are statistical only. Most of the corrections discussed in Sec. III were smaller (and their uncertainties were much smaller) than these statistical errors. The uncertainties in the 1.7 to 2% deuteron absorption correction contributes

TABLE I. Differential cross section for n-p elastic scattering at 647.5 MeV.

θ^* (deg)	$d\sigma/d\Omega^*$ $\left[\frac{\text{mb}}{\text{sr}}\right]$	$-u$ $\left[\frac{\text{GeV}}{c}\right]^2$	$d\sigma/du$ $\left[\frac{\text{mb}}{(\text{GeV}/c)^2}\right]$	θ^* (deg)	$d\sigma/d\Omega^*$ $\left[\frac{\text{mb}}{\text{sr}}\right]$	$-u$ $\left[\frac{\text{GeV}}{c}\right]^2$	$d\sigma/du$ $\left[\frac{\text{mb}}{(\text{GeV}/c)^2}\right]$	θ^* (deg)	$d\sigma/d\Omega^*$ $\left[\frac{\text{mb}}{\text{sr}}\right]$	$-u$ $\left[\frac{\text{GeV}}{c}\right]^2$	$d\sigma/du$ $\left[\frac{\text{mb}}{(\text{GeV}/c)^2}\right]$
179.6	9.19±0.15	0.0000	95.02±1.53	133.7	1.38±0.06	0.1880	14.31±0.60	89.0	0.87±0.04	0.6181	9.02±0.46
178.9	9.04±0.08	0.0001	93.50±0.84	133.0	1.31±0.06	0.1934	13.55±0.58	88.4	0.90±0.05	0.6249	9.27±0.48
178.2	9.06±0.06	0.0003	93.68±0.64	132.3	1.31±0.06	0.1989	13.55±0.58	87.7	0.79±0.05	0.6316	8.21±0.49
177.4	8.73±0.05	0.0006	90.23±0.56	131.6	1.24±0.06	0.2044	12.78±0.58	86.8	0.83±0.05	0.6420	8.62±0.47
176.7	8.59±0.07	0.0010	88.86±0.72	130.9	1.21±0.05	0.2100	12.49±0.55	86.1	0.81±0.05	0.6486	8.37±0.48
176.0	8.34±0.08	0.0015	86.25±0.82	129.1	1.19±0.05	0.2245	12.32±0.53	85.5	0.87±0.04	0.6553	9.04±0.45
175.2	7.77±0.08	0.0021	80.40±0.81	128.4	1.23±0.05	0.2303	12.72±0.54	84.9	1.02±0.05	0.6620	10.51±0.47
174.5	7.35±0.16	0.0028	75.96±1.63	127.7	1.11±0.05	0.2361	11.44±0.52	84.3	0.91±0.05	0.6686	9.36±0.47
174.3	7.15±0.20	0.0030	73.90±2.02	127.0	1.09±0.05	0.2419	11.28±0.51	83.6	1.03±0.05	0.6752	10.69±0.48
173.6	7.10±0.20	0.0038	73.39±2.02	126.3	1.01±0.05	0.2478	10.42±0.51	83.0	1.01±0.05	0.6818	10.43±0.50
172.9	6.36±0.19	0.0047	65.81±1.94	125.6	1.00±0.05	0.2538	10.30±0.49	82.4	1.03±0.05	0.6884	10.67±0.51
172.1	6.53±0.19	0.0057	67.51±1.96	124.9	1.01±0.05	0.2597	10.44±0.50	81.7	0.98±0.05	0.6949	10.12±0.49
171.4	5.86±0.18	0.0068	60.60±1.86	124.2	1.00±0.05	0.2658	10.32±0.49	77.6	1.21±0.06	0.7383	12.47±0.58
170.7	5.64±0.18	0.0080	58.33±1.86	123.6	0.96±0.05	0.2718	9.94±0.49	77.0	1.25±0.06	0.7447	12.95±0.60
170.0	5.50±0.18	0.0093	56.84±1.84	118.3	0.77±0.04	0.3193	8.01±0.40	76.4	1.21±0.06	0.7510	12.52±0.59
169.2	4.98±0.17	0.0107	51.46±1.75	117.6	0.80±0.04	0.3257	8.31±0.38	75.7	1.18±0.06	0.7574	12.24±0.57
168.5	4.77±0.17	0.0122	49.28±1.74	117.0	0.77±0.04	0.3321	7.98±0.41	75.1	1.34±0.06	0.7637	13.90±0.63
165.2	4.17±0.14	0.0202	43.17±1.43	116.3	0.89±0.04	0.3386	9.15±0.41	74.5	1.39±0.06	0.7699	14.39±0.63
164.5	4.14±0.14	0.0222	42.77±1.45	115.6	0.75±0.04	0.3450	7.73±0.42	73.9	1.46±0.06	0.7762	15.09±0.65
163.7	4.18±0.14	0.0243	43.18±1.43	114.9	0.80±0.04	0.3515	8.22±0.42	73.3	1.36±0.06	0.7824	14.09±0.65
163.0	3.98±0.14	0.0265	41.20±1.44	114.3	0.85±0.04	0.3581	8.84±0.41	72.7	1.41±0.06	0.7886	14.56±0.64
162.3	3.84±0.13	0.0288	39.67±1.38	113.6	0.77±0.04	0.3646	7.93±0.39	72.1	1.54±0.06	0.7947	15.93±0.67
161.6	3.86±0.13	0.0312	39.90±1.37	112.9	0.79±0.04	0.3712	8.13±0.41	68.6	1.68±0.07	0.8291	17.35±0.74
160.8	3.63±0.13	0.0337	37.59±1.39	112.2	0.70±0.04	0.3778	7.25±0.40	68.0	1.60±0.07	0.8351	16.53±0.72
160.1	3.69±0.13	0.0363	38.12±1.36	110.8	0.72±0.04	0.3916	7.46±0.37	67.4	1.71±0.08	0.8410	17.73±0.78
159.4	3.64±0.13	0.0389	37.64±1.39	110.2	0.84±0.04	0.3982	8.69±0.38	66.8	1.70±0.07	0.8468	17.54±0.77
157.0	3.25±0.10	0.0481	33.57±1.00	109.5	0.83±0.04	0.4049	8.58±0.38	66.2	1.85±0.08	0.8527	19.14±0.79
156.3	3.16±0.09	0.0512	32.63±0.98	108.8	0.75±0.04	0.4116	7.78±0.37	65.6	1.79±0.08	0.8585	18.48±0.80
155.6	3.17±0.09	0.0543	32.75±0.96	108.2	0.75±0.04	0.4183	7.75±0.37	65.0	1.75±0.07	0.8642	18.12±0.76
154.9	3.03±0.09	0.0575	31.37±0.97	107.5	0.76±0.04	0.4250	7.90±0.38	64.4	1.69±0.08	0.8700	17.49±0.80
154.2	3.13±0.09	0.0608	32.39±0.96	106.8	0.73±0.04	0.4318	7.54±0.37	63.8	1.83±0.08	0.8756	18.98±0.82
153.4	2.89±0.09	0.0642	29.85±0.93	106.2	0.71±0.04	0.4385	7.34±0.36	63.4	2.05±0.08	0.8798	21.22±0.81
152.7	3.09±0.09	0.0676	31.95±0.96	105.5	0.75±0.04	0.4453	7.80±0.39	62.8	2.08±0.08	0.8854	21.52±0.81
152.0	2.78±0.09	0.0712	28.71±0.91	104.8	0.70±0.03	0.4521	7.29±0.36	62.2	2.13±0.08	0.8910	22.01±0.83
145.8	2.19±0.07	0.1053	22.62±0.74	99.3	0.72±0.04	0.5098	7.50±0.45	61.6	2.11±0.08	0.8965	21.79±0.84
145.1	2.20±0.07	0.1096	22.75±0.71	98.6	0.69±0.04	0.5166	7.17±0.44	61.0	2.18±0.08	0.9021	22.55±0.85

TABLE I. (*Continued.*)

θ^* (deg)	$d\sigma/d\Omega^*$ $\left[\frac{\text{mb}}{\text{sr}}\right]$	$-u$ $\left[\frac{\text{GeV}}{c}\right]^2$	$d\sigma/du$ $\left[\frac{\text{mb}}{(\text{GeV}/c)^2}\right]$	θ^* (deg)	$d\sigma/d\Omega^*$ $\left[\frac{\text{mb}}{\text{sr}}\right]$	$-u$ $\left[\frac{\text{GeV}}{c}\right]^2$	$d\sigma/du$ $\left[\frac{\text{mb}}{(\text{GeV}/c)^2}\right]$	θ^* (deg)	$d\sigma/d\Omega^*$ $\left[\frac{\text{mb}}{\text{sr}}\right]$	$-u$ $\left[\frac{\text{GeV}}{c}\right]^2$	$d\sigma/du$ $\left[\frac{\text{mb}}{(\text{GeV}/c)^2}\right]$
144.3	2.15±0.07	0.1140	22.24±0.73	98.0	0.75±0.04	0.5234	7.81±0.46	60.4	2.27±0.08	0.9075	23.47±0.87
143.6	2.06±0.07	0.1184	21.26±0.70	97.3	0.73±0.05	0.5303	7.53±0.48	59.8	2.13±0.08	0.9130	22.06±0.85
142.9	2.00±0.07	0.1229	20.73±0.71	96.7	0.70±0.04	0.5371	7.22±0.45	59.3	2.39±0.09	0.9184	24.67±0.90
142.2	1.99±0.07	0.1275	20.60±0.71	96.0	0.74±0.04	0.5439	7.69±0.46	58.7	2.22±0.08	0.9237	22.96±0.87
141.5	1.98±0.07	0.1322	20.49±0.71	95.4	0.69±0.04	0.5507	7.18±0.44	55.2	2.80±0.10	0.9546	28.93±1.03
140.8	1.91±0.07	0.1369	19.74±0.68	94.7	0.73±0.05	0.5576	7.60±0.47	54.6	2.82±0.10	0.9597	29.20±1.01
140.1	1.72±0.06	0.1417	17.77±0.66	93.5	0.77±0.04	0.5707	7.97±0.44	54.0	2.78±0.10	0.9647	28.70±1.06
139.4	1.65±0.06	0.1465	17.08±0.64	92.9	0.77±0.04	0.5775	8.01±0.42	53.4	2.92±0.10	0.9696	30.15±1.06
137.2	1.52±0.06	0.1618	15.73±0.63	92.2	0.78±0.04	0.5843	8.06±0.43	52.9	2.87±0.11	0.9746	29.69±1.10
136.5	1.44±0.06	0.1669	14.90±0.60	91.6	0.73±0.04	0.5911	7.60±0.43	52.3	3.06±0.11	0.9795	31.68±1.12
135.8	1.51±0.06	0.1721	15.65±0.61	90.9	0.81±0.04	0.5978	8.42±0.45	51.7	3.19±0.11	0.9843	32.94±1.14
135.1	1.47±0.06	0.1773	15.16±0.62	90.3	0.83±0.04	0.6046	8.61±0.45	51.1	3.16±0.12	0.9891	32.70±1.19
134.4	1.41±0.06	0.1826	14.58±0.61	89.7	0.86±0.04	0.6114	8.93±0.46				

negligibly to the normalization uncertainty of 7% (see Sec. II H) which is assigned to the entire angular distribution. As noted in Sec. III B 4, these cross section values can be renormalized if a more accurate value for the $np \to d\pi^0$ total cross section becomes available. As noted in Sec. II I, the uncertainties of θ^* range from $\pm 0.27°$ at $\sim 180°$ to $\pm 0.97°$ at $\sim 50°$.

B. Comparison with other experiments

A comparison of the results of this experiment with the results from PPA[3] and Dubna[4] is presented in Fig. 12, and a comparison with the Saclay results[5] in the charge exchange region is presented in Fig. 13. Our cross section values are seen to fall between those from Dubna and PPA, but they are in reasonably good agreement with the Saclay data except at the largest angles ($\theta^* > 175°$), where a difference in the shape of the backward peak is apparent. A reason for believing that the shape exhibited by the present experimental results is more reliable will be discussed in Sec. IV D. A plausible explanation for possible errors in the Saclay measurements at these extreme back angles is the high counting rates in the scintillator hodoscopes used as detectors in that experiment when in the direct neutron beam.

The data of Ref. 8 are not shown in Fig. 13 because they would distract from the comparison with the Saclay results. Furthermore, that experiment and the one reported here were done with the same apparatus, largely the same techniques, and many of the same personnel and thus is not a completely independent experiment. Not surprisingly, the results reported in Ref. 8 at nearby energies differed very little from the results reported here, except that, on the average, the cross section values of Ref. 8 at 636.2 MeV were slightly larger and those at 660.4 MeV slightly smaller than the 647.5 MeV results reported here.

C. Phase shift fit

Also shown in Figs. 12 and 13 is the differential cross section curve produced by a phase-shift fit labeled C650. This fit was obtained with the computer program of Arndt and VerWest[30] using an extended set of both published and unpublished n-p and p-p data in the 590–709 MeV energy region. The n-p data base included the LAMPF differential cross section data,[6–8] including the present results, but not those from PPA,[3] Dubna,[4] and Saclay.[5] In

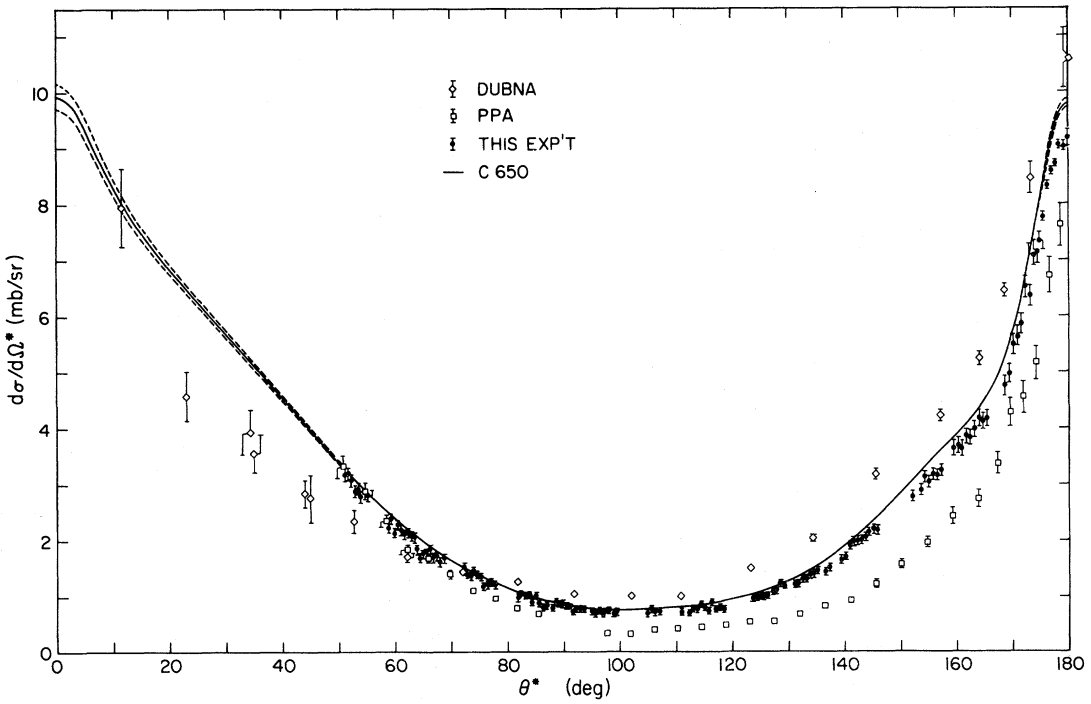

FIG. 12. Comparison of *n-p* differential cross section measurements near 650 MeV. The results of the present experiment (●) at 647.5 MeV are compared with the PPA results (□) (Ref. 3) at 649 MeV, the Dubna results (◇) (Ref. 4) at 630 MeV, and the results of a phase-shift fit, C650 (solid line) obtained with the code of Arndt and VerWest (Ref. 30).

addition, it included total cross section data from Dubna[31] and PPA (Ref. 32); polarization and analyzing power data (*n-p* or *p-n*) from Berkeley,[33,34] Dubna,[35–39] and LAMPF (Refs. 40 and 41); Wolfenstein triple scattering parameter measurements (*n-p* or *p-n*) from Berkeley[42,43] and Dubna (Refs. 35–37, 44, and 45); and an *n-p* spin correlation measurement from LAMPF.[46]

The fit was made with 34 free parameters, including coupling parameters up to ϵ_6 and partial wave phase shifts up to ${}^3J_6$. The $I=1$ phase parameters were determined mostly by the *p-p* data and the $I=0$ parameters by the *n-p* data. The *n-p* data set included 842 points and the χ^2 value for the fit was 727. The error corridors indicated by dashed lines in Figs. 12 and 13 show the range of predictions given by fits for which the value of χ^2 per datum increased by 1.0 above its minimum value. It is clear from Fig. 12 that more and better differential cross section measurements at small angles ($\theta^* < 50°$) are needed in this energy region.

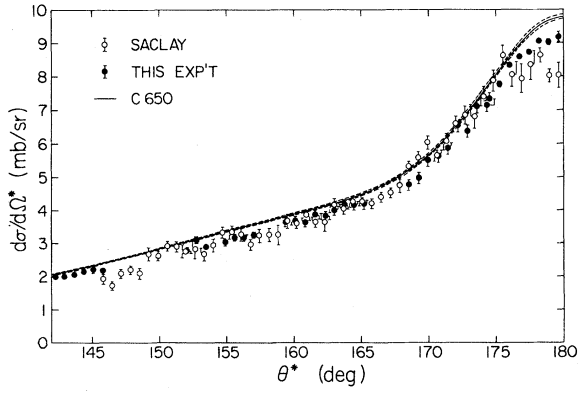

FIG. 13. Comparison of the *n-p* large angle (charge-exchange) differential cross section measurements of this experiment (●) with the Saclay measurements (○) (Ref. 5) at 649 MeV, and with the phase-shift fit C650.

In the χ^2 minimization process it is customary to float the normalization of data from individual experiments. The normalization factor obtained for the present data in fit C650 was 1.0616. This is within the 7% normalization uncertainty we have assigned to these data due to uncertainties in the $pp \rightarrow d\pi^+$ cross section and possible isospin noninvariance.

D. Charge exchange region

The shape of the peak in the backward angle (CE) region is undoubtedly influenced by one-pion exchange (OPE) effects but is not well understood. In

Born approximation the OPE amplitude goes to zero as $-u$ (square of the neutron four-momentum transfer) goes to zero, i.e., as θ^* goes to 180°. A suggested explanation[47] for the presence of a sharp peak rather than a minimum in $d\sigma/du$ at $u=0$ is destructive interference between the OPE amplitude and a slowly varying background amplitude, but a quantitative explanation for the observed shape remains to be given. It has long been known,[48] however, that the shape was well described by the empirical double-exponential formula:

$$\frac{d\sigma}{du}=\alpha_1 e^{\beta_1 u}+\alpha_2 e^{\beta_2 u} . \tag{12}$$

Obtaining values of α_1, α_2, β_1, and β_2 by least-squares fitting to this formula provides a convenient way of comparing the data of the various experiments in the CE region ($145<\theta^*<180°$). The results of such fitting are presented in Table II, along with the values of χ_ν^2 (chi squared per degree of freedom) which measure the goodness of each fit. The parameters obtained for the fits to the data of Ref. 8 are not shown, but are in agreement with those of the present experiment and have comparable uncertainties and χ_ν^2 values. The parameters obtained for the fits to the Dubna, PPA, and Saclay data are not in agreement with each other or with the fitting parameters of the present experiment. The very small χ_ν^2 value for the Dubna data is a consequence of the relatively large error bars of the data and the few degrees of freedom available to the fit. The excellence of the fit to the present data is shown in Fig. 14.

An alternative and more sophisticated way of determining the plausibility of the shape of the backward peak in the angular distribution is to use the pole-extrapolation method of Chew[49] to extract the pion-nucleon coupling constant from this shape. In this energy region the method should give a value which is reasonably accurate.[50] The method is based on the conjecture that there are poles in the real part of the nucleon-nucleon scattering amplitude due to single pion exchange at the unphysical values,

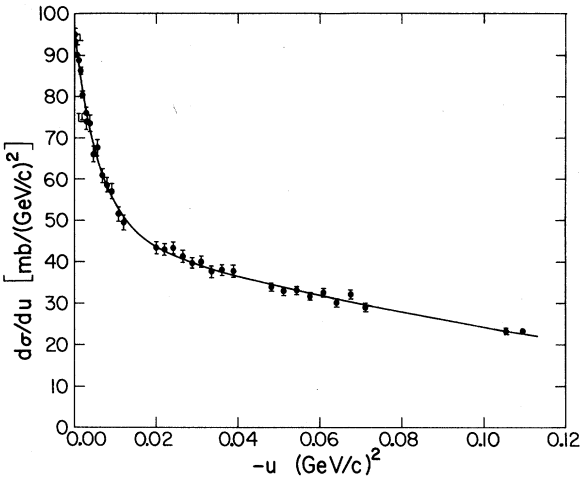

FIG. 14. Double exponential fit to the large angle ($\theta^*>145°$) data of the present experiment, given by the parameters of Table II in Eq. (12).

$$\cos\theta^*=\pm(1+\mu^2/2k^2) ,$$

where μ is the pion rest mass and k is the nucleon c.m. momentum, as well as branch points at

$$\cos\theta^*=\pm(1+4\mu^2/2k^2),\pm(1+9\mu^2/2k^2), \ldots ,$$

owing to higher order processes. For n-p charge-exchange scattering the $(-)$ signs are applicable and μ is the mass of the charged pion. More specifically, the differential cross section may be written[50] in terms of the pion-nucleon coupling constant $g^2=(2m/\mu)^2 f^2$ (m is the neutron rest mass) and the quantity $x=\cos\theta^*+1+\mu^2/2k^2$ as

$$\frac{d\sigma}{d\Omega^*}=\frac{g^4}{4E^2}\frac{(1+\cos\theta^*)^2}{x^2}+\frac{A}{x}+B , \tag{13}$$

where $E=(k^2+m^2)^{1/2}$ is the total energy of the neutron in the c.m. system. The first term in this expression is the one-pion contribution and the other two represent higher order processes. While A and B are unknown functions of x, it is known that they are finite at $x=0$. Thus, from Eq. (13) and the definition of x a new function of x can be generated

TABLE II. Two exponential fits to the charge-excharge data in the 650 MeV energy region.

Expt.	Ref.	T (MeV)	No. of Points	α_1	β_1	α_2	β_2	χ_ν^2
Dubna	4	630	6	54.9±4.5	106±15	56.6±2.8	5.04±0.61	0.12
PPA	3	649	11	40.7±3.5	183±35	37.0±2.2	10.1 ±0.8	0.97
Saclay	5	649	50	38.5±1.7	119±11	45.7±1.6	7.73±0.53	1.85
Present		647.5	36	47.2±1.0	165±8	48.3±1.0	7.06±0.33	0.94

TABLE III. Pion-nucleon coupling constant determination from this experiment.

	$145° \leq \theta^* \leq 180°$			$104° \leq \theta^* \leq 180°$		
	χ_ν^2	$P(n)$	f^2	χ_ν^2	$P(n)$	f^2
2	22.07		imaginary	19.36		imaginary
3	4.704	1.00	0.0418±0.0015	10.59	1.00	imaginary
4	1.133	1.00	0.0650±0.0020	7.444	1.00	0.0183±0.0024
5	1.010	0.97	0.0742±0.0042	2.559	1.00	0.0489±0.0014
6	1.043	0.06	0.0749±0.0102	1.216	1.00	0.0639±0.0017
7	1.078	0.14	0.0712±0.0234	1.099	1.00	0.0695±0.0023
8				1.001	1.00	0.0759±0.0030
9				1.010	0.41	0.0740±0.0048
10				1.023	0.24	0.0723±0.0073

$$y(x)=x^2\frac{d\sigma}{d\Omega^*}$$
$$=\frac{g^4}{4E^2}(x-\mu^2/2k^2)^2+Ax+Bx^2 \qquad (14)$$

in which the last two terms containing the unknown functions A and B vanish as x goes to zero, yielding

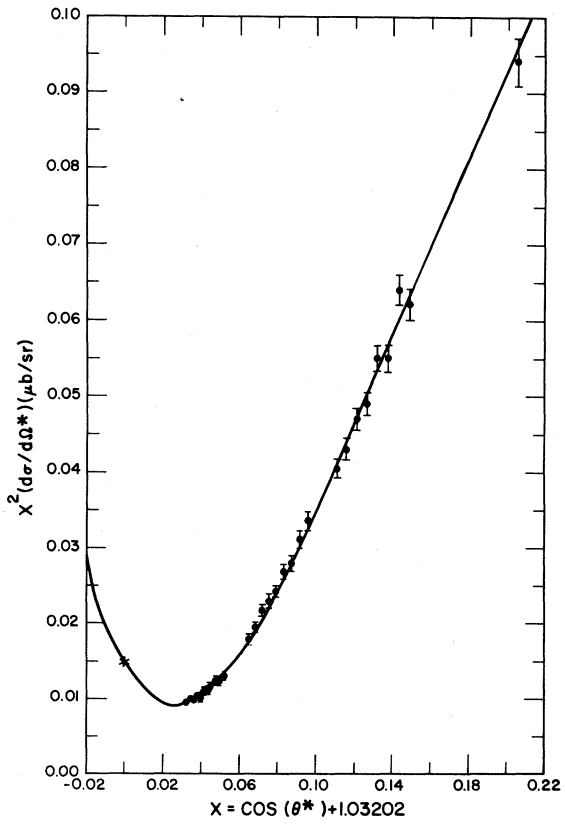

FIG. 15. Five term polynomial fit of Eq. (16) to values of the function $\chi^2(d\sigma/d\Omega^*)$ calculated from the large angle ($\theta^* > 145°$) cross section data of the present experiment. The fit is extrapolated to the pion pole in the unphysical region (shown by *) to determine the pion-nucleon coupling constant [Eq. (17)].

$$y(0)=\frac{g^4}{4E^2}\left[\frac{\mu^2}{2k^2}\right]^2=\frac{f^4m^4}{k^4(k^2+m^2)} . \qquad (15)$$

Since values of x smaller than $\mu^2/2k^2$ are unphysical, the value of $y(0)$ is obtained by extrapolation of $y(x)$ from the physical region. This is done by making a least-squares fit of the n-term polynomial

$$f(x)=\sum_{i=0}^{n-1} a_i x^i \qquad (16)$$

to the physical values of $y(x)$ calculated with Eq. (14), and taking $y(0)=f(0)=a_0$, yielding

$$f^2=[a_0(k^2+m^2)]^{1/2}(k/m)^2 . \qquad (17)$$

Two sets of polynomial fits were made, one for the angular range of the double exponential fit discussed above, $145° < \theta^* < 180°$, and the other for the larger angular range $104° < \theta^* < 180°$. For each set the number of terms in the polynomial was varied from 2 to 10, and two criteria were used to determine the optimum number of terms. The first was that χ_ν^2 be a minimum. The second was a determination by means of the F test[51] of whether the inclusion of another term in the polynomial significantly improves the fit. In this test the probability $P(n)$, that addition of the nth term to the expansion results in significant reduction of χ_ν^2, is calculated. As n is increased, $P(n)$ should be near 1.0 as long as the added terms are improving the fit, but a sharp drop in the value of $P(n)$ indicates that the nth term did not improve the fit and is not needed. Ideally, the same number of significant terms should be indicated by the χ_ν^2 minimum and the dropoff of $P(n)$.

The values obtained for χ_ν^2, $P(n)^2$, and f^2 for the polynomial fits to data in the two angular regions, for increasing numbers of terms, are presented in Table III. It will be noted that, for each data set the

TABLE IV. Comparison of pion-nucleon coupling constant determinations obtained from n-p data in the charge-exchange region ($\theta^* > 145°$) near 650 MeV.

Expt.	Ref.	No. of Data	n	χ_ν^2	$P(n+1)$	f^2
Dubna	4	6	4	0.020	0.38	0.0521 ± 0.0089
PPA	3	11	5	1.085	0.29	0.0717 ± 0.0117
Saclay	5	50	8	1.190	0.07	imaginary
Saclay[a]	5	44	5	1.178	0.49	0.0501 ± 0.0133
Present		36	5	1.010	0.06	0.0742 ± 0.0042

[a]Excluding the six points with $\theta^* > 176°$.

number of significant terms indicated by both criteria is the same, $n=5$ for the smaller angular range and $n=8$ for the larger. This optimum fit for the smaller angular range is shown in Fig. 15. The values of the pion-nucleon coupling constant f^2 given by the two data sets are in agreement. The value $f^2=0.0759\pm0.0030$ given by the more extended set is presumed to be the better value, largely because the dropoff in $P(n)$ near the χ^2 minimum is more abrupt for that set. This value of f^2 is in good agreement with values scattered about $f^2=0.08$ obtained from analysis of pion-nucleon scattering; a recent determination[52] yields $f^2=0.0769\pm0.0020$. It also is in agreement with the value $f^2=0.0762\pm0.0043$ obtained from a phase-shift analysis of p-p scattering data.[53]

It is of interest to use this same procedure to determine the f^2 values given by previous n-p CE cross section measurements in this energy region.[3–5] In Table IV, the results obtained in such an analysis for the angular region $145° < \theta^* < 180°$ are compared with the result given by this experiment. The most reasonable value of f^2 and that with the smallest statistical uncertainty is the one given by this experiment. With one exception, the goodness of the fit was measured by χ_ν^2 is also best for the present data. The small value of χ_ν^2 for the fit to the Dubna data comes from the very few degrees of freedom in the fit, and the value of f^2 obtained is far from the accepted value. The fact that the value of f^2 obtained from the Saclay data is imaginary if all of the data are included but more reasonable if the data for $\theta^* > 176°$ are omitted reinforces the belief that those back-angle points are suspect, and that the shape of the angular distribution in the CE region is that indicated by the present experiment.

V. CONCLUSIONS

It appears that previous discrepancies have been resolved and that the n-p differential cross section in this energy region is well determined for angles $50° < \theta^* < 180°$. There is relatively good agreement in the CE region between the present data, those from Saclay (excluding six points for $\theta^* > 176°$), and those of Ref. 8. A good value is extracted for the pion-nucleon coupling constant from the present experiment, and there is relatively good agreement over the entire angular range $50° < \theta^* < 180°$ between the data of this experiment and the phase-shift prediction, both in shape and normalization (within our normalization uncertainty). More and better measurements are needed, however, for the forward angle region $0° < \theta^* < 50°$. Nonetheless, the present results together with recent LAMPF analyzing power[40,41] and spin correlation[46] results have considerably reduced the ambiguities that previously existed in the n-p $I=0$ scattering matrix.[30]

ACKNOWLEDGMENTS

We would like to thank J. G. Boissevain, D. Brown, and S. Cohen for their help in development of the MWPC spectrometer system and electronics, J. H. Fretwell and K. D. Williamson for their help in the development and operation of the LD_2 neutron production target, A. C. Niethammer for her contribution to development of the data acquisition code, and the LAMPF staff for numerous forms of assistance during the course of the experiment. This work was performed mostly under the auspices of U. S. Energy Research and Development Administration and the U. S. Department of Energy.

*Present address: Schlumberger Well Services, P.O. Box 2175, Houston, TX 78228.

†Present address: Los Alamos National Laboratory, Los Alamos, NM 87545.

‡Present address: Science Applications, Inc., LaJolla, CA 92037.

§Present address: c/o Landis X Gyr-3574, 6301 Zug, Switzerland.

[1]R. A. Arndt, R. H. Hackman, and L. D. Roper, Phys. Rev. C 15, 1002 (1977).

[2]R. DuBois *et al.*, Nucl. Phys. A377, 554 (1982).

[3]P. F. Shepard, T. J. Devlin, R. E. Mischke, and J. Solomon, Phys. Rev. D 10, 2735 (1974).

[4]Yu. M. Kazarinov, F. Lehar, and Yu. N. Simonov, Joint Institute for Nuclear Research Report P-1207, 1963; quoted by J. Bystricky and F. Lehar in *Physics Data,* (Fachinformationszentrum, Karlsruhe, 1978), p. 502.

[5]G. Bizard, F. Bonthonneau, J. L. Laville, F. LeFebvres, J. C. Malherbe, and R. Regimbart, Nucl. Phys. B85, 14 (1975). After publication, these data were renormalized (G. Bizard, private communication). The values as tabulated in the compilation of Bystricky and Lehar (Ref. 4, p. 505) have been further renormalized. From a comparison of the renormalizations it appears that two of the values in the compilation have been misprinted; i.e., the value at $\theta^* = 157.45°$ should be 3.23 rather than 2.23 mb/sr, and the value at $\theta^* = 175.48°$ should be 8.63 rather than 6.63 mb/sr.

[6]M. L. Evans *et al.*, Phys. Rev. Lett. 36, 497 (1976).

[7]M. L. Evans, Ph.D. thesis, Texas A&M University, 1976; available as Los Alamos National Laboratory Report LA-7733-T, 1979 (unpublished).

[8]B. E. Bonner, J. E. Simmons, C. L. Hollas, C. R. Newsom, P. J. Riley, G. Glass, and M. Jain, Phys. Rev. Lett. 41, 1200 (1978).

[9]W. Hürster, Th. Fischer, G. Hammel, K. Kern, M. Kleinschmidt, L. Lehmann, H. Schmitt, L. Schmitt, and D. M. Sheppard, Phys. Lett. 90B, 367 (1980).

[10]A. J. Bersbach, R. E. Mischke, and T. J. Devlin, Phys. Rev. D 13, 535 (1976).

[11]R. Carlini *et al.*, Phys. Rev. Lett. 41, 1341 (1978).

[12]R. K. Keeler *et al.*, Nucl. Phys. A377, 529 (1982).

[13]C. W. Bjork *et al.*, Phys. Lett. 63B, 31 (1976).

[14]G. Glass *et al.*, Phys. Rev. D 15, 36 (1977).

[15]L. C. Northcliffe, in Proceedings of the International Conference on the Interaction of Neutrons with Nuclei, Lowell, Massachusetts, 1976, Energy Research and Development Administration Report Conf-760715-P1, 1976, p. 808; W. Thomas *et al.*, Phys. Rev. D 24, 1736 (1981); B. E. Bonner *et al.*, Phys. Rev. C 18, 1418 (1978).

[16]K. D. Williamson, J. E. Simmons, F. J. Edeskuty, J. H. Fretwell, J. T. Martin, and H. Ficht, *Advances in Cryogenic Engineering* (Plenum, New York, 1974), Vol. 19, p. 241.

[17]A. J. Tallerico, Los Alamos National Laboratory Report LA-UR-900, 1974 (unpublished).

[18]D. W. Werren *et al.*, Los Alamos National Laboratory Report LA-5396-MS, 1973 (unpublished).

[19]G. Charpak, Annu. Rev. Nucl. Sci. 20, 195 (1970).

[20]R. Bouclier, G. Charpak, Z. Dimčovski, G. Fischer, F. Sauli, G. Coignet, and G. Flügge, Nucl. Instrum. Methods 88, 149 (1970).

[21]G. Charpak, H. G. Fischer, C. R. Gruhn, A. Minten, F. Sauli, G. Plch, and G. Flügge, Nucl. Instrum. Methods 99, 279 (1972).

[22]D. Brown, Nucl. Instrum. Methods 117, 561 (1974).

[23]L. R. Biswell and R. E. Rajala, Los Alamos National Laboratory Report LA-4916-MS, 1972 (unpublished).

[24]J. C. Hiebert and A. C. Niethammer, Los Alamos National Laboratory Report LA-5609-MS, 1974 (unpublished).

[25]C. Richard-Serre, W. Hirt, D. F. Measday, E. G. Michaelis, M. J. M. Saltmarsh, and P. Skarek, Nucl. Phys. B20, 413 (1970).

[26]D. F. Measday, private communication.

[27]M. Hutchinson, J. Friedman, and A. Rittenberg, University of California Radiation Laboratory Group A, Programming Note No. P-171, 1973 (unpublished).

[28]M. Jain, M. L. Evans, and L. C. Northcliffe, Nucl. Phys. A336, 325 (1979).

[29]J. D. Seagrave, *The Three Body Problem* (North-Holland, Amsterdam, 1970), p. 69.

[30]R. A. Arndt and B. J. VerWest, in *Polarization Phenomena in Nuclear Physics—1980 (Fifth International Symposium, Santa Fe),* Proceedings of the Fifth International Symposium on Polarization Phenomena in Nuclear Physics, AIP Conf. Proc. No. 69, edited by G. G. Ohlsen, R. E. Brown, N. Jarmie, M. W. McNaughton, and G. M. Hale (AIP, New York, 1981), p. 179.

[31]V. P. Dzhelepov, V. I. Satarov, and B. Golovin, Dokl. Akad. Nauk SSSR 104, 717 (1955).

[32]T. J. Devlin, W. Johnson, J. Norem, K. Vosburgh, R. E. Mischke, and W. Schimmerling, Phys. Rev. D 8, 136 (1973).

[33]D. Cheng, B. MacDonald, J. A. Helland, and P. M. Ogden, Phys. Rev. 163, 1470 (1967).

[34]K. Leung, private communication to R. A. Arndt.

[35]Yu. Bagaturia *et al.*, Joint Institute for Nuclear Research Report P1-12143, 1979.

[36]Yu. M. Kazarinov, F. Lehar, A. F. Pisarev, and Z. Janout, Yad. Fiz. 5, 140 (1967) [Sov. J. Nucl. Phys. 5, 97 (1967)].

[37]S. I. Bilenkaya, L. N. Glonti, Yu. M. Kazarinov, and V. S. Kiselev, Joint Institute for Nuclear Research Report P1-4690, 1970.

[38]V. P. Dzhelepov, B. M. Golovin, V. S. Nadeshdin, and V. I. Satarov, Proceedings of the XIIth International Conference on High Energy Physics, Dubna, 1964, Vol. I, p. 11.

[39]R. Zulkarneev, Kh. Murtazaev, and V. Khachaturov, Phys. Lett. 61B, 164 (1976).

[40]C. R. Newsom *et al.*, in *Polarization Phenomena in Nuclear Physics—1980 (Fifth International Symposium, Santa Fe),* Proceedings of the Fifth International Symposium on Polarization Phenomena in Nuclear Physics, AIP Conf. Proc. No. 69, edited by G. G. Ohlsen, R. E. Brown, N. Jarmie, M. W. McNaughton, and G. M. Hale (AIP, New York, 1981), p. 126; C. R. Newsom, private communication to R. A. Arndt.

[41]T. S. Bhatia, private communication to R. A. Arndt.

[42]P. H. Surko, Ph.D. thesis, University of California Radiation Laboratory Report 19451, 1970.

[43]K. Leung, Ph.D. thesis, University of California Radiation Laboratory Report 19704, 1970.

[44]L. N. Glonti, Yu. M. Kazarinov, and M. R. Khayatov, Zh. Eksp. Teor. Fiz. 62, 1998 (1972) [Sov. Phys.—JETP 35, 1042 (1972)].

[45]B. M. Golovin, V. P. Dzhelepov, V. S. Nadezhdin, and V. I. Satarov, Zh. Eksp. Teor. Fiz. 36, 433 (1959) [Sov. Phys.—JETP 9, 302 (1959)]; see also Ref. 36.

[46]T. S. Bhatia *et al.*, in *Polarization Phenomena in Nuclear Physics—1980 (Fifth International Symposium, Santa Fe),* Proceedings of the Fifth International Symposium on Polarization Phenomena in Nuclear Physics, AIP Conf. Proc. No. 69, edited by G. G. Ohlsen, R. E. Brown, N. Jarmie, M. W. McNaughton, and G. M. Hale (AIP, New York, 1981), p. 123; T. S. Bhatia, private communication to R. A. Arndt.

[47]R. J. N. Phillips, Phys. Lett. 4, 19 (1963).

[48]J. L. Friedes, H. Palevsky, R. L. Stearns, and R. J. Sutter, Phys. Rev. Lett. 15, 38 (1965).

[49]G. F. Chew, Phys. Rev. 112, 1380 (1958).

[50]P. Cziffra and M. J. Moravcsik, Phys. Rev. 116, 226 (1959).

[51]P. R. Bevington, *Data Reduction and Error Analysis for the Physical Sciences* (McGraw-Hill, New York, 1969), Chap. X.

[52]V. K. Samaranayake, J. Phys. G 5, 657 (1979).

[53]M. H. MacGregor, R. A. Arndt, and R. M. Wright, Phys. Rev. 169, 1128 (1968).